FEDSM2022-86967

HYDRODYNAMICS OF METACHRONAL MOTION: EFFECTS OF SPATIAL ASYMMETRY ON THE FLOW INTERACTION BETWEEN ADJACENT APPENDAGES

Zhipeng Lou¹, Adrian Herrera-Amaya², Margaret L. Byron², Chengyu Li¹

¹ Villanova University, Villanova, PA 19085, USA

² Pennsylvania State University, University Park, PA 16802, USA

ABSTRACT

Metachronal motion is a unique swimming strategy widely adopted by many small animals on the scale of microns up to several centimeters (e.g., ctenophores, copepods, krill, and shrimp). During the propulsion, the evenly spaced appendages perform a propulsive stroke sequentially with a constant phaselag from its neighbor, forming a metachronal wave. In order to produce the net thrust in the fluid regime that viscous force is dominant, the beat cycle of a metachronal appendage presents significant spatial asymmetry. As the Reynolds number increases, the metachronal motion changes from high spatial asymmetry to lower spatial asymmetry. The varying kinematics of the metachronal motion will inevitably affect the flow interaction between adjacent appendages. However, it is still unclear how the magnitude of spatial asymmetry can modify the shear layers near the tip of appendages and thus affect its associated hydrodynamic performance. In this study, Ctenophores are used to investigate the hydrodynamics of multiple appendages in the metachronal wave. Unlike other ciliated invertebrates, Ctenophore cilia are grouped into paddlelike structures (i.e., ctenes), which beat metachronally in rows circumscribing an ovoid body. Based on high-speed video recordings, we reconstruct the metachronal wave of ctenes for a lower spatial asymmetry case and a higher spatial asymmetry case, respectively. An in-house immersed-boundary-methodbased computational fluid dynamics solver is utilized to simulate the flow field and associated hydrodynamic performance. Our simulation results aim to provide fundamental fluid dynamic principles for guiding the design of bio-inspired miniaturized flexible robots swimming in the low-to-intermediate Reynolds number regime.

NOMENCLATURE

F_{T}	Thrust force
F_{L}	Lift force
C_{T}	Thrust coefficient
C_{L}	Thrust coefficient
C_p	Thrust coefficient
η	Power efficiency
$ar{U}_{\it tip}$	Mean ctenes tip velocity
L_{ctene}	Ctene mean length
L_{body}	Body length of the ctenophore
S	Ctenes surface area
f	Flapping frequency
$Re_{_{\omega}}$	Reynolds number
u_{i}	Velocity component
p	Pressure
ν	Seawater kinematic viscosity
T	One cycle period

1. INTRODUCTION

Metachronal wave can be commonly found among small swimming organisms [1, 2] which equipped with cilium structure or swimming legs (e.g., paramecium, ctenophores,

copepods, krill, and shrimp). By using a drag-based propulsion strategy, the closely spaced appendages sequentially execute a power stroke followed by a recovery stroke to generate fluid momentum in the direction of animal motion. Two key features of the metachronal paddling can be characterized as the phase lag between adjacent appendages [3] and spatiotemporal asymmetric locomotion of individual appendage [4]. Specifically, the appendage interacts with each other and is stimulated by its neighboring appendages sequentially, forming the metachronal wave. The spatiotemporal asymmetry is the result of the fluid-structure interactions and the stiffness difference during the power stroke and the recovery stroke. The propulsion is achieved during the power stroke when the appendage beats oppositely against the swimming direction. In general, the period of power stroke is always shorter than the recovery stroke, which creates a temporal asymmetry during each beating cycle [4].

Most of the species using ciliary-like propulsion are microscales. In the time-reversible flow regime (Re \ll 1), the spatial asymmetric stroke is necessary to produce net fluid displacement for a cilium [5]. In addition, the phase lag between adjacent appendages also play an important role in driving flow [6]. At low-to-intermediate Reynolds number (10° <Re<10²), however, the level of spatiotemporal asymmetry may vary significantly on ciliary propulsion. Adrian et al. [7] experimentally measured the spatial and temporal asymmetry behavior of ctenophores' strokes across a wide range of Reynolds numbers (Re \approx 20 \sim 200). Their results indicated that the level of spatial asymmetry decreases with the increasing Reynolds number, while the temporal asymmetry is more pronounced at higher Reynolds number.

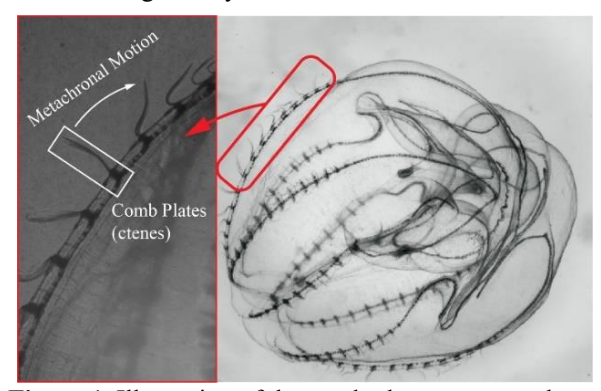


Figure 1. Illustration of the comb plates on ctenophore.

Ctenophore, the largest animals in the world which locomote via cilia, is thus an ideal species to study ciliary propulsion in the low-to-intermediate flow regime [8]. Unlike micro-scale cilia that occur collective beating behavior in carpets, cilia of the ctenophore are grouped into paddle-like structures (ctenes), which beat metachronally in rows circumscribing an ovoid body. In addition, cilia of the ctenophore are lined by eight separate rows. These explicit and transparent cilia arrays can provide clear enough sights for visualization in the experimental measurements. The interaction among the widely spaced eight

rows of ctenes can be ignored, so each row can be studied individually [9].

In this study, models of ctenophores with different body sizes are reconstructed based on high-speed videos. The reconstructions are performed in Autodesk MAYA. All models contain one row of ctenes and exclude the rotational motion and twisting of ctenes. An in-house immersed-boundary-method-based computational fluid dynamics solver is utilized to simulate the flow field and associated hydrodynamic performance. Based on the simulation results, we demonstrated how the effects of the spatial asymmetry influence the propulsion and the inter-ctenes interaction. Our simulation and analysis aim to improve our understanding of fundamental flow physics of ciliary propulsion and provide guidance for the design of bio-inspired miniaturized flexible robots swimming in the low-to-intermediate Reynolds number regime.

2. METHODOLOGY

2.1 Morphological parameter and 3D reconstruction model

In this study, *Bolinopsis vitrea* were collected at Flatt's Inlet, Bermuda and transported to the Bermuda Institute of Ocean Sciences. The experiments were operated in 12 hours after the animal collection. The swimming condition is prepared in seawater which was seeded with phytoplankton. The morphological parameters of Ctenophore used in this study are listed in Table 1. More details of the filming experiments are described in the Ref.[7].

Table 1. Morphological parameters of the ctenophores

Parameters	Small	Large	
rarameters	animal	animal	
Body length, L_{body} (mm)	11.56	42	
Ctene mean length, L_{ctene} (mm)	0.63	0.76	
Ctene beat frequency, f (Hz)	17.85	15.32	
Oscillatory Reynolds number, Re_{ω}	43.39	52.92	
Spatial Asymmetry Index, Sa	0.49	0.29	

After a sequence of images obtained, one array of the ctenes is treated as reference and reconstructed into 3D model in Autodesk MAYA. Since the ctenes are bands of fused cilia on the ctenophore bodies, each band in the array is reconstructed as one single comb plate that has no camber and twisting (see Figure 1). Any global translation and rotation of the ctenophore are eliminated. Then, the selected row of the ctenes and the basal substructure are relocated perpendicularly in a Cartesian coordinate for simulations.

2.2 Appendage kinematics

In viscous-dominated fluid, the viscosity of the medium will affect the metachronal pattern of the appendage array. The influence of the viscosity change was characterized as the spatiotemporal difference of the ciliary cycle [4]. Based on the main interest in this study, we focus on the spatial change

resulting from metachronal motion at different Reynolds numbers. The spatial asymmetric kinematic of ctene motion is illustrated in Figure 2. To quantitatively evaluate the level of spatial asymmetry of each appendage, an asymmetry parameter, spatial asymmetry index, is defined in equation (1) according to Ref. [7]).

$$Sa = \frac{A_e}{A_o}; (1)$$

where A_e is the area enclosed by the tip trajectory over one cycle, and the A_o is the area of an inscribed ellipse within a half-circle whose length is the L_{ctene} . This ellipse represents an approximation for the maximum reachable area of each ctene's tip considering its flexibility. Based on the definition, a Sa value of 1 implies an asymmetric stroke cycle when the tip passes maximum reachable location in one cycle. A zero value of Sa indicates a completely symmetric stroke motion of the ctene when power stroke has identical path as recovery stroke.

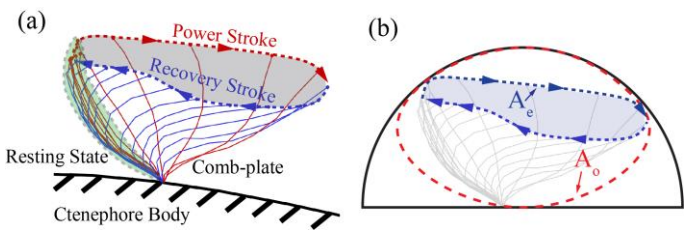


Figure 2. Kinematics illustration of the ctenes in an orthogonal lateral view. The blue solid line represents one appendage during a time series of the recovery stroke. The red solid line represents the same appendage doing power stroke. The doted blue curve and the red one indicates the tip trajectory of each stroke.

Other than the spatial asymmetry, the temporal asymmetry can also be observed, which means the comb-plate power stroke quicker than the recovery stroke. But before the power stroke, there is a rest period when the cilia got itself stiffen (Figure 2a). This resting stage was previously observed by Parducz [10]. It is the result of the unilateral contraction of the cilia root.

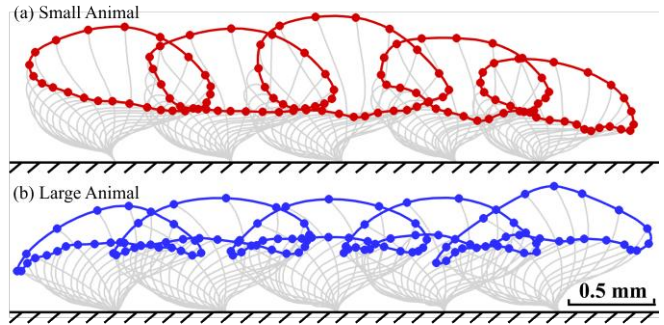


Figure 3. The cilia tip trajectory of for the (a) smaller ctenophore (model I), (b) larger ctenophore (model II).

Figure 3 illustrates the tip trajectory of two models that are reconstructed. For oval tip trajectory (model I) in Figure 3a, the Sa is 0.49 which refers to high asymmetric strokes. During the recovery stroke, the tips remain low distance with respect to the body surface. In Figure 3b, the tip trajectory of the larger ctenophore (model II) appears similar to an airfoil. The lower trajectory presents more chamber and farther from the body surface. The mean Sa for the cilia is 0.29 which indicates more spatial symmetric stroke cycles.

For both models, each ctene shows a phase lag of the instant velocity to the adjacent ctene. To examine the kinematics of all ctenes, we remove all the phase lags to obtain the mean instant velocity for each model. Figure 4a present the mean instant velocity of model I which strokes asymmetrically, and Figure 4b describes the mean instant velocity of model II. The peak velocity of the model II is higher than that of the model I. The model II also has the lower bound of velocity. The period of the power stroke for both models is around 41% of one cycle. This shows an agreement with the temporal asymmetry parameters summarized by Adrian et al. [7].

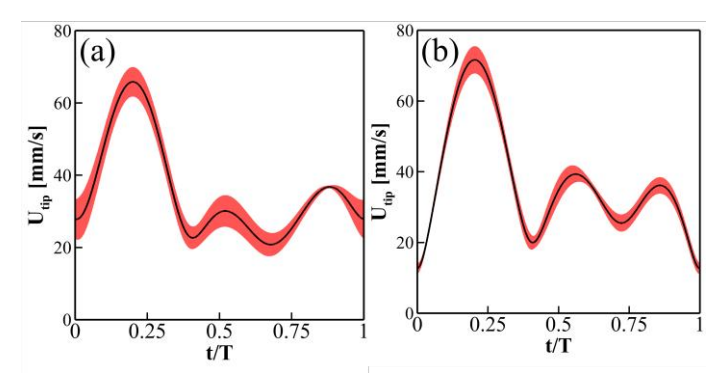


Figure 4. Time courses of cilia tip velocity for (a) small ctenophore (model I) and (b) large ctenophore (model II). The solid black curve represents the time history obtained by averaging five cilium tips for each animal after removing the phase shift. The red shaded margins of the curves show the standard deviation.

2.3 Governing equations and numerical method

The governing equations adopted here are the unsteady incompressible viscous Navier-Stokes equations, which is shown in equation (2), and discretized using the collocated grid arrangement, where the primitive variables (u_i and p) are stored in the cell center.

$$\frac{\partial u_{i}}{\partial x_{i}} = 0;$$

$$\frac{\partial u_{i}}{\partial t} + \frac{\partial (u_{i}u_{j})}{\partial x_{i}} = -\frac{\partial p}{\partial x_{i}} + \frac{1}{Re} \frac{\partial}{\partial x_{i}} (\frac{\partial u_{i}}{\partial x_{i}})$$
(2)

where u_i (i = 1,2,3) are the velocity components in the x-, y-, and z-directions, respectively; p is the pressure, and Re is the Reynolds number.

The above equations are solved by a finite difference-based immersed-boundary method in a non-body-conforming Cartesian grid, which are integrated with time using the fractional step method. The advantage of immersed-boundary method is that it is not necessary to use complicated re-meshing algorithms that are used by other conventional body conformal methods. Details of the CFD solver in solving Navier–Stokes equations are elaborated and validated in our previous studies [11-14].

2.4 Simulation setup

The reconstructed model is placed in a non-uniform Cartesian grid. The total grid size is 4.91 million which has the dimension of $337\times113\times129$. There is a denser mesh layer right around the model and a less dense mesh layer wrapping the denser mesh region. The most outside layer of meshes are stretched from the secondary layer to the boundary. In front of the bare substructure, the inflow comes in. The outflow condition boundary condition is applied for the back of the flow region. And the rest of the boundaries are set as zero-gradient boundary conditions. The oscillatory Reynolds number is used for this study which is given by $Re_{\omega}=2\pi f L_{cilia}^2/\nu$. And the value is calculated based on the parameters in Table 1 and the values of Re_{ω} are 42.39 and 52.92, respectively, for the high spatial asymmetry case and low spatial asymmetry case. To achieve periodic steady results, four complete cycles are simulated.

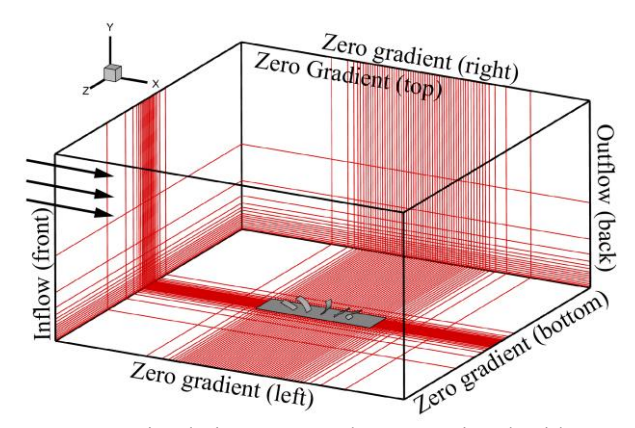


Figure 5. Simulation setup and computational grids.

RESULTS AND DISCUSSIONS

By solving the Navier-Stokes equations, the surface pressure and the shear stress are computed, which can be further integrated into hydrodynamic forces of each ctenes. To evaluate the overall hydrodynamic performance, we calculated the thrust coefficient (see Figure 6). Here, the thrust and lift coefficients (C_T and C_L) are obtained from the horizontal and vertical forces along the inflow and given by equation (4) and (5).

$$C_{T} = \frac{F_{T}}{\frac{1}{2}\rho \overline{U}_{up}^{2} S}; \tag{4}$$

$$C_{L} = \frac{F_{L}}{\frac{1}{2}\rho \overline{U}_{up}^{2}S} \tag{5}$$

where ρ is the water density, $\overline{U}_{_{\mathit{ip}}}$ is the mean ctenes tip velocity, and S is the surface area of each ctene.

The hydrodynamic power is calculated by the surface integral of the product of the pressure and velocity of each surface element, which is defined by equation (6). The power coefficient is given by equation (7) and the power efficiency is defined by equation (8).

$$P = -\iint p\mathbf{n} \cdot \mathbf{u}_c ds \tag{6}$$

$$C_{p} = \frac{P}{\frac{1}{2}\rho \overline{U}_{np}^{3} S} \tag{7}$$

$$\eta = \frac{C_T}{C_P} \tag{8}$$

where u_c is the cell-centered velocity vector; n is the unit vector that is normal to the surface of a small area ds.

The simulations are performed for both model I and model II. First, we calculated the thrust coefficients of each appendage which overlaps in Figure 6 colored separately. From the first appendage a to the last appendage, C_{τ} of each appendage presents a phase lag to adjacent ones. For instance, appendage b has a phase lag of C_{τ} against appendage a, and meanwhile appendage c has a phase lag of C_{τ} against appendage b. By comparison between two animals, the peak thrust of the spatial symmetrical model is higher than that of the asymmetrical model. Also, the spatial symmetrical model faces larger peak drag force. To be more quantitative, the cycle-averaged values of

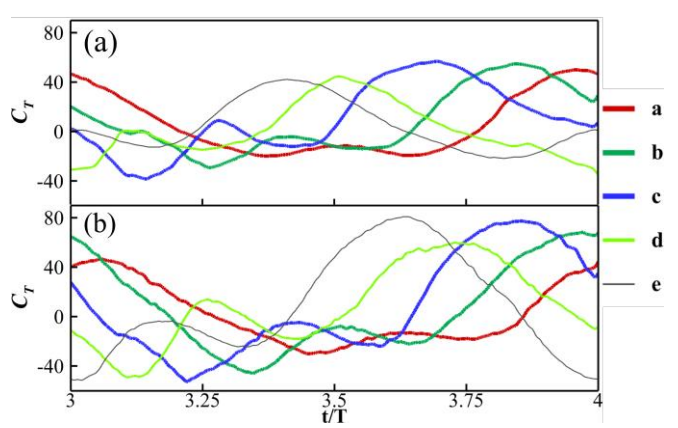


Figure 6. The time history of thrust coefficient C_{τ} for spatial symmetrical and asymmetrical models. (a) Smaller ctenophore (model I). (b) Larger ctenophore (model II). Appendages a to e are labeled the front to the back of the flow region.

thrust coefficient \overline{C}_T are summarized in Table 2. The mean \overline{C}_T of spatial symmetrical model produces more overall thrust, which is 15% more than that of spatial asymmetrical model.

Figure 7 presents the power coefficient of two models. The phase lags among appendages can also be observed. The power consumed by more spatial symmetrical stroke (Figure 7a) is as almost twice as that by more asymmetrical stroke (Figure 7b).

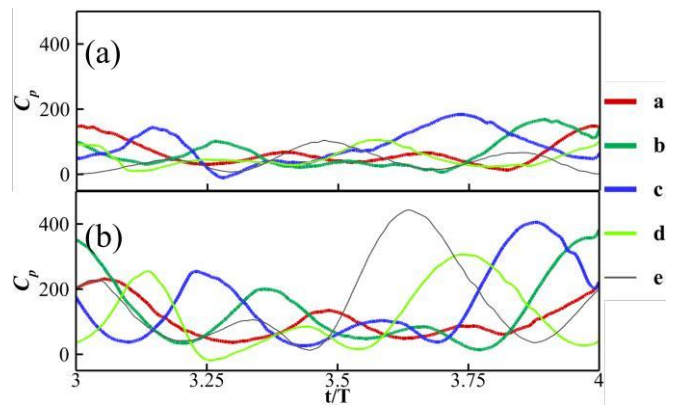


Figure 7. The time history of power coefficient C_p for spatial symmetrical and asymmetrical models. (a) Smaller ctenophore (model I). (b) Larger ctenophore (model II). Appendages a to e are labeled the front to the back of the flow region.

The power coefficients are summarized in in Table 2. Model II which strokes more symmetrically consumes 118% more than the model I which strokes more asymmetrically. The power efficiency for producing thrust is also compared in the last two columns. Model I has 9.27% power efficiency and $\bar{\eta}$ of model II is 4.90%. Therefore, model I has 47% better efficiency for thrust production.

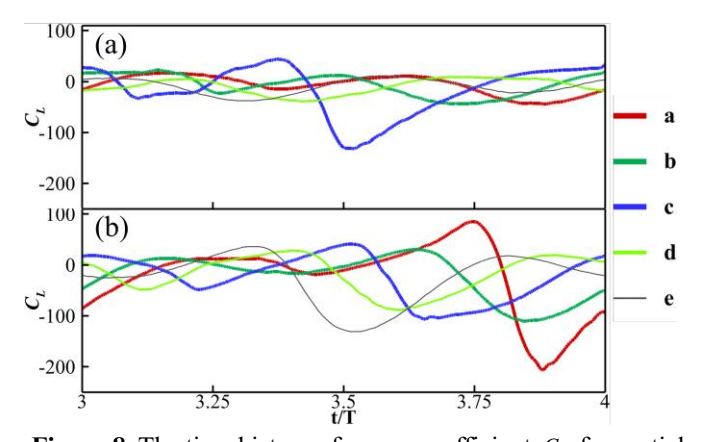


Figure 8. The time history of power coefficient C_p for spatial symmetrical and asymmetrical models. (a) Smaller ctenophore (model I). (b) Larger ctenophore (model II). Appendages a to e are labeled the front to the back of the flow region.

The spatial symmetrical model is able to produce more thrust which results in a super high cost of power. However, the model II does not consume 118% additional power to only achieve 15% more thrust than the model I. After evaluating the lift coefficient C_{τ} in Figure 8, we found that more negative lift is created by the symmetry stroke of model II. In Table 2, model II generated 134% more normal force towards the body surface. As a result, the majority of the power is contributed to the surface pressure on the body.

Table 2. The comparison of hydrodynamic performances between high spatial asymmetrical case (model I) and low spatial asymmetrical case (model II).

	\bar{C}_T		$ar{C}_L$		\overline{C}_{P}		$\overline{\eta}$ [%]	
	I	П	I	II	I	II	I	II
a	5.31	1.73	-6.52	-22.80	63.48	104.55	8.36	1.65
b	7.85	6.34	-6.81	-22.51	65.03	132.07	12.08	4.80
c	9.67	7.53	-16.67	-25.05	85.20	152.55	11.35	4.93
d	1.08	8.15	-9.24	-18.38	49.62	116.79	2.17	6.97
e	4.26	8.70	-9.78	-26.24	40.44	156.37	10.53	5.56
AVE	5.63	6.49 (+15%)	-9.80	-23.00 (+134%)	60.75	132.47 (+118%)	9.27	4.90 (-47%)

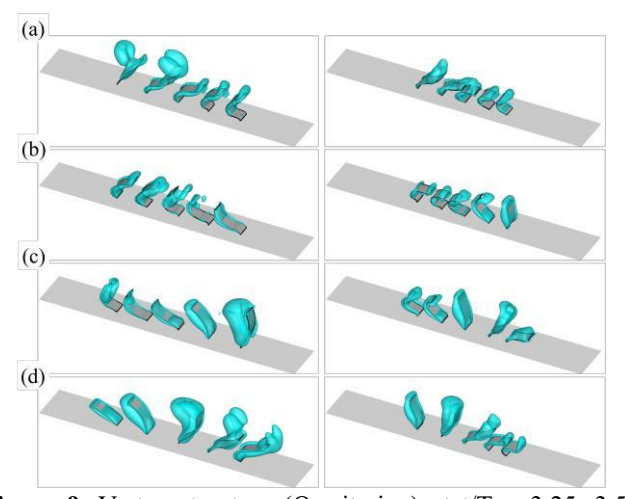


Figure 9. Vortex structure (Q-criterion) at t/T = 3.25, 3.5, 3.75, 4, respectively. The left column shows smaller ctenophore (model I) and the right column shows the larger ctenophore (model II).

To investigate the vortex formation, we visualized the 3D vortex structures by Q-criterion. Figure 9 provides the perspective view of the vortex structures generated by two models at four instants during a beating cycle. The phase lag of

wake structure can be observed. At the first 3/4 cycle (Figure 9c), the ctene c is in the power phase. Then, at the end of the cycle (Figure 9d), the adjacent ctene e is doing power stroke. The power stroke of front ctene follows the next adjacent ctene.

Figure 10 shows the contour of the lateral vorticity and the velocity is represented by the arrows. When one ctene strokes in power phase, a vortex is generated on the ctene tip. The vortex formation is similar to the leading-edge vortex of flapping wings [15]. These tip vortices observed here was also observed in other studies regarding the ctenophores [7, 16].

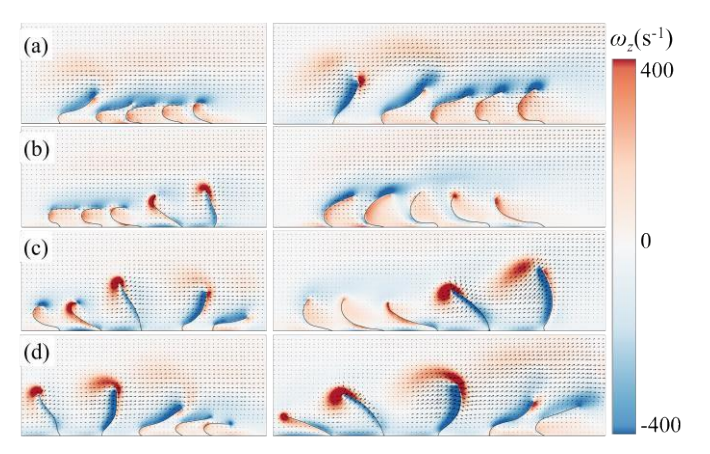


Figure 10. Contour of lateral vorticity at t/T = 3.25, 3.5, 3.75, 4, respectively. The left column shows smaller ctenophore (model I) and the right column shows the larger ctenophore (model II).

By comparing the kinematics and associated hydrodynamic performance between a smaller ctenophore and a larger ctenophore, our results indicated that the smaller ctenophore adopts more spatial asymmetry metachronal motion than the larger ctenophore. When the size of the ctenophore increases while the other conditions remain the same, the Reynolds number increases correspondingly, which causes the stroke pattern to change. Take a study of Paramecium as an instance, when viscosity increases, the direction of its power stroke changes gradually [17]. Similarly, when Reynolds number changes, the ctenophore changes its swimming strategy, which actively adjusts the kinematics and its associated hydrodynamic performance. The additional normal force on body found in this study is an example that when the body size gets larger, the ctenophore creates more body pressure based on the swimming technique of each individual animal. Because of the ovoid body geometry in nature, the normal force component generated by the model II can also contribute a force component along its body moving direction. This hypothesis also provides possible explanations for the hydrodynamics effects of the ctenophore's body geometry.

CONCLUSIONS

In this study, the hydrodynamic performance of metachronal rowing is quantitatively evaluated using an immersed-boundarymethod-based CFD solver. The effects of different levels of spatial asymmetry on hydrodynamics are investigated. For both the smaller ctenophore (model I, Sa=0.49, high spatial asymmetry) and larger ctenophore (model II, Sa=0.29, low spatial asymmetry), the power stroke period is around 41% of the whole beat cycle. Our simulation results showed that the low spatial asymmetric case (model II) produces 15% more thrust while consuming 118% more power than the high spatial asymmetric model (model I). The additional power consumption of the low spatial asymmetric case is found mostly contribute to the generation of normal force component, which is perpendicular to the substrate surface. Therefore, the power efficiency for thrust production of the low asymmetric case is 47% lower than the high asymmetric case. This observation suggests that the low spatial asymmetric beating potentially generates more force in the intermediate Reynolds number regime. However, it also inevitably creates a big force component normal to the substrate, which is not desired for the thrust-to-power ratio. In nature, the substrate geometry of the ctenophore is curved. We hypothesize that such a curved substrate may compensate for the thrust-to-power ratio of the low asymmetric beating pattern since it potentially reorientates the normal force component along its body moving direction.

ACKNOWLEDGMENTS

This research was supported by the National Science Foundation to C. Li (NSF CBET-2120505) and to M. L. Byron (NSF CBET-2120689). All simulations were run on the High-Performance Computing Cluster of the College of Engineering at Villanova University.

REFERENCES

- [1] M. L. Byron, D. W. Murphy, K. Katija, A. P. Hoover, J. Daniels, K. Garayev, et al., "Metachronal motion across scales: current challenges and future directions," *Integrative and comparative biology,* vol. 61, pp. 1674-1688, 2021.
- [2] M. Byron, A. Santhanakrishnan, and D. Murphy, "Metachronal Coordination of Multiple Appendages for Swimming and Pumping," *Integrative and comparative biology*, vol. 61, pp. 1561-1566, 2021.
- [3] S. Chateau, J. Favier, S. Poncet, and U. D'Ortona, "Why antiplectic metachronal cilia waves are optimal to transport bronchial mucus," *Phys Rev E,* vol. 100, p. 042405, Oct 2019.
- [4] J. Han and C. S. Peskin, "Spontaneous oscillation and fluid-structure interaction of cilia," *Proc Natl Acad Sci U S A*, vol. 115, pp. 4417-4422, Apr 24 2018.
- [5] E. M. Purcell, "Life at low Reynolds number E. M. Purcell

Citation:," American Journal of Physics, vol. 45, 1977.

- [6] D. Takagi, "Swimming with stiff legs at low Reynolds number," *Phys Rev E Stat Nonlin Soft Matter Phys*, vol. 92, p. 023020, Aug 2015.
- [7] A. Herrera-Amaya, E. K. Seber, D. W. Murphy, W. L. Patry, T. S. Knowles, M. M. Bubel, *et al.*,

- "Spatiotemporal Asymmetry in Metachronal Rowing at Intermediate Reynolds Numbers," *Integr Comp Biol*, vol. 61, pp. 1579-1593, Nov 17 2021.
- [8] S. L. Tamm, "Cilia and the life of ctenophores," *Invertebrate Biology*, vol. 133, pp. 1-46, 2014.
- [9] W. L. Heimbichner Goebel, S. P. Colin, J. H. Costello, B. J. Gemmell, and K. R. Sutherland, "Scaling of ctenes and consequences for swimming performance in the ctenophore
- Pleurobrachia bachei," Invertebrate Biology, vol. 139, 2020.
- [10] B. Párducz, "Ciliary Movement and Coordination in Ciliates," ed, 1967, pp. 91-128.
- [11] C. Li, H. Dong, and G. Liu, "Effects of a dynamic trailing-edge flap on the aerodynamic performance and flow structures in hovering flight," *Journal of Fluids and Structures*, vol. 58, pp. 49-65, 2015.
- [12] C. Li and H. Dong, "Wing kinematics measurement and aerodynamics of a dragonfly in turning flight," *Bioinspiration & Biomimetics*, vol. 12, p. 026001, 2017.
- [13] C. Li, H. Dong, and K. Zhao, "A balance between aerodynamic and olfactory performance during flight in Drosophila," *Nature Communications*, vol. 9, pp. 1-8, 2018.
- [14] C. Li, J. Jiang, H. Dong, and K. Zhao, "Computational modeling and validation of human nasal airflow under various breathing conditions," *Journal of Biomechanics*, vol. 64, pp. 59-68, 2017.
- [15] A. R. J. Jeff D. Eldredge, "Leading-Edge Vortices: Mechanics and Modeling," *Annu. Rev. Fluid. Mech*, vol. 51, 2019.
- [16] S. P. Colin, J. H. Costello, K. R. Sutherland, B. J. Gemmell, J. O. Dabiri, and K. T. Du Clos, "The role of suction thrust in the metachronal paddles of swimming invertebrates," *Sci Rep*, vol. 10, p. 17790, Oct 20 2020.
- [17] H. MACHEMER, "Ciliary Activity and the Origin of Metachrony in Paramecium: Effects of Increased Viscosity," vol. 57, pp. 239-259, 1972.